Author(s): Bazhenov, Andrey; Honkala, Karoliina

Title: Understanding Structure and Stability of Monoclinic Zirconia Surfaces from First-Principles Calculations

Year: 2017

Version:

Please cite the original version:

Bazhenov, A., & Honkala, K. (2017). Understanding Structure and Stability of Monoclinic Zirconia Surfaces from First-Principles Calculations. Topics in Catalysis, 60(6), 382-391. https://doi.org/10.1007/s11244-016-0701-0

Topics in Catalysis manuscript No.
(will be inserted by the editor)

Understanding Structure and Stability of Monoclinic Zirconia Surfaces from First-Principles Calculations

Andrey S. Bazhenov · Karoliina Honkala

Received: date / Accepted: date

Abstract Under the water-rich pre-treatment and/or reaction conditions, structure and chemistry of the monoclinic zirconia surfaces are strongly influenced by oxygen vacancies and incorporated water. Here, we report a combined first-principles and atomistic thermodynamics study on the structure and stability of selected surfaces of the monoclinic zirconia. Our results indicate that among the studied surfaces, the most stable $(\bar{1}11)$ surface is the least vulnerable towards oxygen vacancies in contrast to the less stable (011) and $(\bar{1}01)$ surfaces, where formation of oxygen vacancies is energetically more favorable. Furthermore, we present a vigorous, systematic screening of water incorporation onto the studied surfaces. We observe that the greatest stabilization of the surfaces is achieved when a part of the adsorbed water molecules is dissociated. Nevertheless, the importance of water dissociation for achieving the greatest stabilization is high for the less stable (011) and $(\bar{1}01)$ surfaces, while completely hydrated $(\bar{1}11)$ surface is stabilized equally regardless of the water dissociation state. Analysis of the constructed phase diagrams reveals that the $(\bar{1}11)$ surface remains preferably clean and the (011) and $(\bar{1}01)$ surfaces have dissociated water at low coverage under the reactive conditions of $T = 600$–900 K and $p(H_2O) < 1$ bar. Upon temperature decrease and/or pressure increase, all studied surfaces gradually uptake water until fully hydrated. All in all, our findings complement and broaden the existing picture of the structure and stability of the monoclinic zirconia surfaces under the pre-treatment and/or reaction conditions, enabling rationalization of the potential roles of zirconia as a heterogeneous support and a catalyst component.

Nanoscience Center, Department of Chemistry, FI-40014 University of Jyväskylä, Finland
Tel.: +358 40 8053686
E-mail: karoliina.honkala@jyu.fi

Keywords heterogeneous catalysis, oxide support, reforming, water–gas shift, density functional theory calculations, atomistic thermodynamics, phase diagrams

1 Introduction

Zirconia (zirconium dioxide, ZrO_2) belongs to a large group of irreducible oxides. Due to its unique properties, zirconia acts as a heterogeneous support and a catalyst component in multiple important processes for obtaining sustainable chemicals, as has been highlighted in the recent reviews and reports. [17, 21, 4, 26, 25, 11, 37] Moreover, zirconia finds its applications in, for instance, solid oxide fuel cells [32] and electrochemical sensors. [22] Zirconia exists in several polymorphic modifications, among which monoclinic (*m*), tetragonal (*t*), and cubic (*c*) are the most common examples. The *m*-ZrO_2 crystal form, also known as the mineral baddeleyite, is the most stable at the temperatures below 1480 K, whereas the *t*- and *c*-forms are stable at significantly higher temperature regimes and transform to the monoclinic modification upon cooling.

Zirconia is typically exposed to the water-rich pre-treatment and/or reaction conditions, where adsorption of water on the surfaces of the crystallites may affect their structure [19, 33] and stability [41, 18] and even alter the properties of the surface sites. [20, 44] In particular, zirconia has been extensively studied as a support and a catalyst in reforming processes, [13, 12, 14, 10, 9] where the water–gas shift cycle and the formate formation from CO and water are the key steps. Nonetheless, understanding of the performance of zirconia in the process remains incomplete. Thus, atomic-level understanding of the structure and stability of the zirconia surfaces in the presence of water would be beneficial for clarifying the potential roles of zirconia for reforming processes. Systematic evaluation of the structural

features, such as oxygen vacancies, surface hydration, surface steps and kinks, cannot be achieved by experimental techniques alone. Computational chemistry and molecular modeling have proven to be useful tools to complement the experiments as they consider systems a priori at the atomic level.

Computational evaluation of oxygen vacancies has been primarily reported for the high-temperature polymorphs of zirconia stabilized by dopants (see, for example, Refs. [39, 43, 29, 5, 2, 3]), focusing significantly less on the most stable m-ZrO_2 form. Foster et al. reported an evaluation of charged and neutral vacancies in the m-ZrO_2 bulk. [7] Syngantseva et al. have reported a study on oxygen vacancies formed in the $(\bar{1}11)$ and $(\bar{1}01)$ m-ZrO_2 surfaces. [40] Nonetheless, the study has been limited by consideration of the topmost oxygen atoms alone, ignoring the possibility of vacancies to be present in the subsurface atomic layers.

Some computational studies exist that deal with stability and hydration of the m-ZrO_2 surfaces. A few research groups have reported water adsorption on the most abundant low-index m-ZrO_2 surfaces, such as $(\bar{1}11)$, $(\bar{1}01)$, and (111), to be dissociative at low surface coverage. [15, 19] Piskorz et al. have performed computational studies on surface hydration and equilibria of m- and t-ZrO_2. [30, 31] The authors have reported significant stabilization of the $(\bar{1}11)$, (111), (011), and (001) surfaces of m-ZrO_2 upon adsorption of water. Moreover, water incorporation has shown to exhibit polymodal character, meaning that the m-ZrO_2 surfaces uptake water in a step-wise manner. Furthermore, at higher values of the surface coverage, the strongest stabilization of the m-ZrO_2 surfaces and, hence, strongest chemisorption of water have been characterized by partial dissociation of molecules. The aforementioned studies have only accounted for a rather limited number of surface/water complexes. The authors have generated the structures by using the most stable configurations under low water content, where water is preferably dissociated, and incorporated additional molecules of water thereto. This have led to neglecting the complexes, where, for example, water is adsorbed solely in molecular mode or dissociated completely. Therefore, a more systematic and thorough screening of the m-ZrO_2/$(H_2O)_x$ structures would complement the current picture.

Herein, we present a combined first-principles and atomistic thermodynamcis study on the structure and stability of three low-index m-ZrO_2 surfaces, namely $(\bar{1}11)$, (011), and $(\bar{1}01)$, in presence of oxygen vacancies and water. A systematic evaluation of formation of single oxygen vacancies into the selected surfaces and m-ZrO_2 bulk is performed, thereby accounting for all possible single oxygen vacancies. We examine stability of the m-ZrO_2 surfaces upon gradual incorporation of water and carefully screen through all possible arrangements of the H_2O/OH+H species on the selected surfaces. Finally, a set of most stable structures for each water content is chosen to construct surface phase diagrams to account for the ambient temperature and water pressure. Overall, our results provide a more complete atomic-level understanding of the structure and stability of the selected m-ZrO_2 surfaces. The approach is readily expandable to include other most abundant low-index surfaces as well as other ZrO_2 modifications.

2 Computational Details

2.1 Electronic Structure Calculations

Periodic density functional theory (DFT) calculations were carried out throughout the study using the GPAW 0.11.0 implementation. [6, 24] The Perdew–Burke–Ernzerhof (PBE) functional [27, 28] was employed for all calculations. Sufficiency of the generalized gradient approximation (GGA) in describing electronic structure of irreducible oxides has been demonstated by Ganduglia-Pirovano et al. [8] The core electrons of Zr and O atoms were represented with the PAW setups in the frozen-core approximation. All calculations included 12 valence electrons for each Zr atom, 6 valence electrons for each O atom, and 1 valence electron for each H atom. The m-ZrO_2 bulk was optimized within the $P2_1/c$ space group with the cutoff energy of 700 eV. The reciprocal space was sampled with the $(6 \times 6 \times 6)$ Monkhorst–Pack mesh of k-points. The m-ZrO_2 bulk was allowed to fully relax until the maximum residual force has been below 0.025 eV Å^{-1}, resulting in the structure with $a = 5.161$ Å, $b = 5.231$ Å, $c = 5.340$ Å, and $\beta = 99.6^\circ$, which differs from the experimental data [42, 23] by 0.8% at most and is consistent with other computational results. [30, 19, 18]

The m-ZrO_2 surfaces were constructed from the optimized bulk as (1×1) two-dimensional slabs of four atomic layers thick (16 ZrO_2 units per computational cell), with the two bottom layers (8 ZrO_2 units) fixed at the ideal bulk positions. The surface slabs were surrounded by the sufficient amount of vacuum along the non-periodic direction to ensure the decay of the wave function within the computational cell. Wavefunctions were described on a real space grid with the maximum spacing of 0.20 Å (see Supporting Information for the convergence tests). The reciprocal space was sampled with a $(4 \times 4 \times 1)$ Monkhorst–Pack mesh of k-points. Each structure was allowed to relax on the corresponding potential energy surface until the maximum residual force has been below 0.05 eV Å^{-1}.

2.2 Energetics of Incorporation of Water and Formation of Oxygen Vacancies

The surface energy of a slab, e_S, calculated solely based on the total energy, can be estimated as

$$e_S = \frac{1}{A}\left(E_S - kE_{bulk}\right) - e_{fix}, \tag{1}$$

where E_S and E_{bulk} are the total energies of the surface slab and the bulk, respectively, k is an integer that equalizes the number of ZrO_2 units in the slab and the bulk, A is the surface area of the computational cell, and e_{fix} is the surface energy of a slab with all atoms fixed at the original bulk positions, which is a necessary correction to account for the fixed bottom half of the slab. The quantity e_{fix} is thus calculated as

$$e_{fix} = \frac{1}{2A}\left(E_{fix} - kE_{bulk}\right), \tag{2}$$

where E_{fix} is the total energy of the slab with all atoms fixed at the original bulk positions.

When any modification to the slab is made, such as incorporation of water and/or generation of oxygen vacancies, its surface energy changes by the value Δe_S, which is calculated as

$$\Delta e_S = \frac{1}{A}\underbrace{\left(E_\Sigma - E_S - \sum_i n_i E_i\right)}_{\Delta E}, \tag{3}$$

where E_Σ is the total energy of the modified slab and E_i is the reference energy of i^{th} modification (H_2O or vacancy) present in the amount of n_i molecules/vacancies per computational cell. In the case of incorporation of water, E_i is the total energy of the isolated gas-phase water molecule. In the case of generation of an oxygen vacancy, we take E_i to be the total energy of the oxygen atom in the isolated gas-phase water, i. e. $E_i = E(H_2) - E(H_2O)$, which is a natural reference for the reforming reaction conditions. The quantity in the parentheses in eq 3, ΔE, constitutes either the adsorption energy of water or the formation energy of an oxygen vacancy.

2.3 Atomistic Thermodynamics Calculations

In the present study, we consider temperature, T, and pressure, p, effects by means of the atomistic thermodynamics [34, 35, 36] only for the incorporation of water. The thermodynamic surface energy of a slab, γ_S, can be calculated using an equation similar to eq 1:

$$\gamma_S(T,p) = \frac{1}{A}\left(G_S(T,p) - kG_{bulk}(T,p)\right) - \gamma_{fix}(T,p), \tag{4}$$

where $G_S(T,p)$ and $G_{bulk}(T,p)$ are the free energies of the slab and the m-ZrO_2 bulk, respectively.

We made an assumption that the contributions of non-electronic terms to the partition functions of the periodic slab and bulk are small and approximated $G_S(T,p) \approx E_S$ and $G_{bulk}(T,p) \approx E_{bulk}$, which led to $\gamma_S(T,p) \approx e_S$. Nevertheless, this assumption cannot be applied to eq 3 as one needs to account for the vibrational degrees of freedom of water:

$$\Delta\gamma_S(T,p) = \frac{1}{A}\left(G_\Sigma(T,p) - G_S(T,p) - n\mu_W(T,p)\right), \tag{5}$$

where $G_\Sigma(T,p)$ is the free energy of the slab–water complex, $G_S(T,p) \approx E_S$ is the free energy of the bare slab, and $\mu_W(T,p)$ is the chemical potential of the gas-phase water, which is present in the amount of n molecules per computational cell.

In the case of the slab–water complex, we account for the vibrational degrees of freedom of water via the zero-point energy correction, meaning that $G_\Sigma(T,p) \approx E_\Sigma + E_\Sigma^{ZPE}$. In the case of the gas-phase water molecule,

$$\mu_W(T,p) = E_W + E_W^{ZPE} + \underbrace{\mu_W^\circ(T) + k_B T \ln\frac{p}{p^\circ}}_{\Delta\mu_W(T,p)}, \tag{6}$$

where E_W and E_W^{ZPE} are the total electronic and zero-point vibrational energies of the gas-phase water molecule, $\mu_W^\circ(T)$ is the standard chemical potential taken directly from the NIST-JANAF thermochemical tables, [1] and k_B is the Boltzmann constant. Overall, eqs 4–6 provide the necessary tools for generation of the m-ZrO_2/H_2O phase diagrams, accounting via $\Delta\mu_W(T,p)$ for the ambient temperature and the partial pressure of water.

3 Results and Discussion

3.1 Structures of m-ZrO_2 Bulk and Surfaces

In the m-ZrO_2 bulk, the atoms feature their highest coordination: the zirconium atoms are seven-coordinated, one half of the oxygen atoms are three-coordinated, and the other half of the oxygen atoms are four-coordinated. Among the considered $(\bar{1}11)$, (011), and $(\bar{1}01)$ surfaces of m-ZrO_2, each has four zirconium atoms and five oxygen atoms in the topmost layer of its computational cell. The coordination of the surface zirconium and oxygen atoms is reduced compared to the atoms in the bulk. The $(\bar{1}11)$ surface exposes three six-coordinated and one seven-coordinated surface zirconium atoms. The (011) and $(\bar{1}01)$ surfaces have similar surface structure, featuring one five-coordinated, one six-coordinated, and two seven-coordinated zirconium atoms in the topmost surface layers. The coordination numbers of the surface oxygen atoms are the same for each surface: one

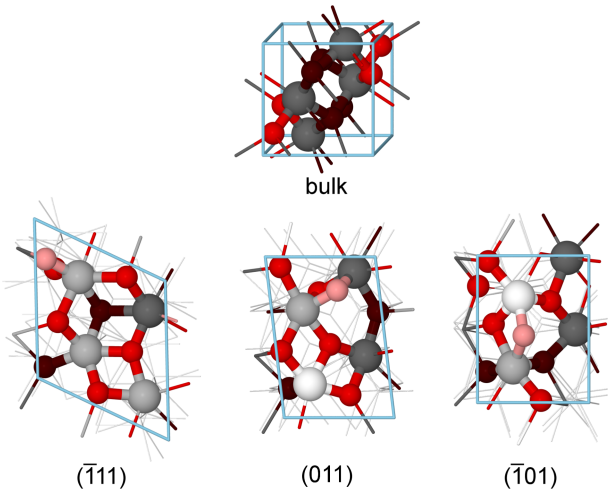

Fig. 1 Structures of the m-ZrO_2 bulk and the representative surfaces. Color coding: seven-coordinated Zr in dark grey, six-coordinated Zr in grey, five-coordinated Zr in white, four-coordinated O in dark red, three-coordinated O in red, two-coordinated O in pink. The computational cells are shown in light blue.

Table 1 Comparison of the m-ZrO_2 surface energies (meV Å^{-2}) calculated relative to the bulk to the literature data.

Surface	present work	literature values
$(\bar{1}11)$	47.7	54.3[a]; 76.3[b]; 76.4[c]
(011)	63.3	83.6[a]
$(\bar{1}01)$	111.0	76.8[a]; 100.6[b]; 96.6[c]

[a] Ref. [30]; [b] Ref. [16]; [c] Ref. [19]

two-coordinated and four three-coordinated atoms per computational cell. Fig. 1 highlights the difference in the coordination of the zirconium and oxygen atoms in the bulk and the studied surfaces. The difference in the coordination of the surface atoms is further reflected in the calculated surface energies (e_S), which increase in a row $(\bar{1}11) < (011) \ll (\bar{1}01)$ as $47.7 < 63.6 \ll 111.0$ meV Å^{-2}.

The calculated surface energies for the m-ZrO_2 surfaces are in reasonable agreement with the previous computational results (Table 1). The observed misalignment could be attributed to multiple factors, among which the most important is the choice of the lowest energy termination for the (011) and $(\bar{1}01)$ surfaces. This might be a rather challenging task due to the complexity of the m-ZrO_2 crystal structure. Additionally, the level of theory as well as the size and stoichiometry of the computational cells might contribute to the determination of the surface energy. Finally, evaluation of the surface energy should include corrections to account for the fixed bottom parts of the surface slabs, which mimic the bulk environment and, consequently, introduce artificial increases to the surface energy values.

Table 2 Formation energies (in eV) of single oxygen vacancies in the studied m-ZrO_2 systems calculated relative to the energy of the oxygen atom in a water molecule.

System	^2O_S	^3O_S	^3O_B	^4O_B
$(\bar{1}01)$ surface	3.24	2.95	3.49	3.25
(011) surface	3.45	3.32	3.40	3.13
$(\bar{1}11)$ surface	3.68	3.63	3.53	3.38
m-ZrO_2 bulk	—	—	3.67	3.58

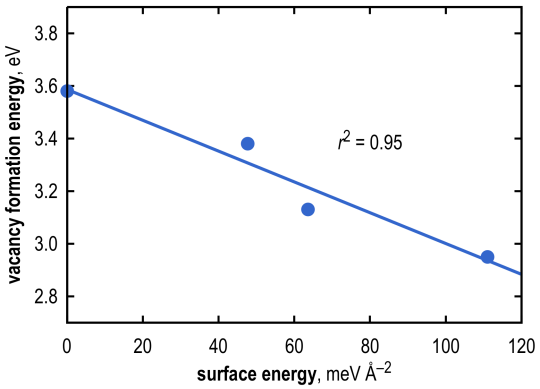

Fig. 2 Formation energies of the most stable oxygen vacancies calculated relative to the energy of the oxygen atom in a water molecule as a function of the corresponding surface energy calculated relative to the m-ZrO_2 bulk.

3.2 Formation of Single Oxygen Vacancies

We started with examining formation energies of single oxygen vacancies in the considered m-ZrO_2 surfaces and compared them to those in the bulk. Both unique lattice sites were considered in the case of the bulk. For the surfaces, the vacancy formation was examined in the surface atomic layers as well as the first subsurface layers, where the coordination of the atoms is one step closer to that of the atoms in bulk. Designation of the lattice sites relevant for discussion is presented as follows: ^3O_B and ^4O_B stand for respective three- and four-coordinated oxygen atoms in the bulk or subsurface atomic layers and ^2O_S and ^3O_S denote respective two- and three-coordinated oxygen atoms in the surface atoms layers.

Table 2 summarizes the energies required for formation of a single oxygen vacancy depending on the location and coordination of the lattice site. In the m-ZrO_2 bulk, formation of an oxygen vacancy at the ^4O_B site is more favorable than at the ^3O_B site by approximately 0.1 eV, which is consistent with the reports by Syzgantseva et al. [40] and Forster et al. [7] This tendency withholds for the subsurface atomic layers of the m-ZrO_2 surfaces; however, the preference of the ^4O_B sites becomes more clear with the differences of >0.15 eV compared to the ^3O_B sites. In the surface layers of

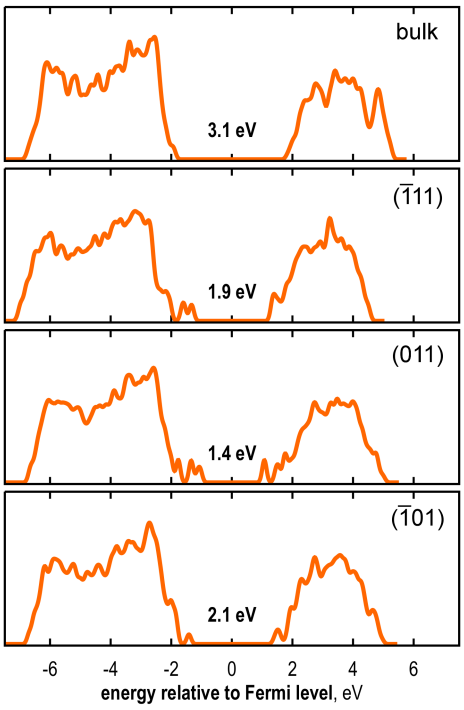

Fig. 3 Calculated density of states plots for the m-ZrO_2 bulk and the studied surfaces. The values on the plots give estimates of the band gap.

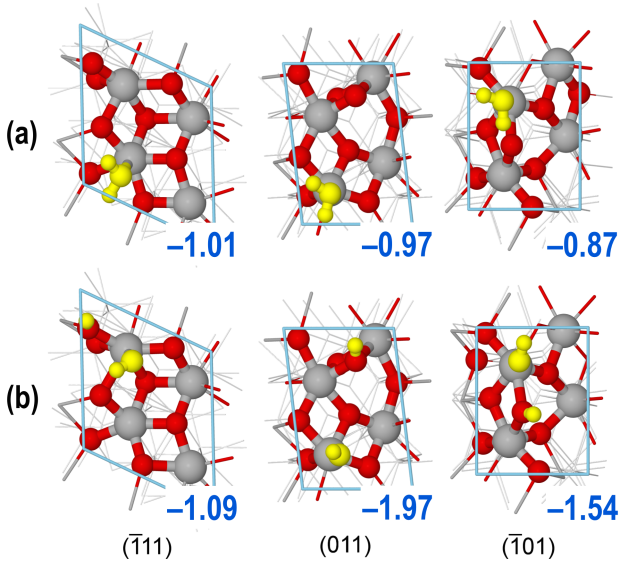

Fig. 4 Structures of the most favorable complexes of the studied surfaces with a single water molecule adsorbed (a) molecularly and (b) dissociatively. Color coding: Zr in grey, O in red, H_2O in yellow. The computational cells are shown in light blue. The numbers in dark blue correspond to the values of the adsorption energy (in eV). For the coordination of the surface atoms, the reader is kindly referred to Fig. 1.

the m-ZrO_2 surfaces, formation of oxygen vacancies at the ^3O_S sites is more preferable compared to the ^2O_S. Syzgantseva et al. [40] have reported an opposite trend; however, the authors considered different spin states of the defective surfaces. Interestingly, the difference in the vacancy formation energy at the ^2O_S and ^3O_S sites ranges from $<$0.05 eV for the most stable $(\bar{1}11)$ surface to $>$0.25 eV for the least stable $(\bar{1}01)$ surface.

In the $(\bar{1}01)$ surface, energetically the least expensive oxygen vacancies are formed at the ^3O_S sites in the surface layer. However, for the $(\bar{1}11)$ and (011) surfaces, the most stable vacancies are formed at the ^4O_B sites in the subsurface layers. The formation energies of the most stable oxygen vacancies showed a strong linear dependence ($r^2 = 0.95$) on the corresponding surface energies (Fig. 2), indicating an overall tendency for oxygen vacancies to be formed at lower energy expenses in less stable surfaces. We observed an overall tendency for the vacancy formation energies for the subsurface layers to generally increase in a row $(011) < (\bar{1}01) < (\bar{1}11)$ and approach the bulk. For the surface layers, the vacancy formation energies increase in a different row, $(\bar{1}01) < (011) < (\bar{1}11)$. Regardless of the vacancy location, the most stable $(\bar{1}11)$ surface is the least vulnerable towards oxygen vacancies.

Fig. 3 presents states plots for the perfect m-ZrO_2 bulk and the studied $(\bar{1}11)$, (011), and $(\bar{1}01)$ surfaces. The calculated band gap for the m-ZrO_2 bulk is 3.1 eV, which agrees with the previous computational [40, 7] results and is slightly underestimated compared to the experimental values of 4.2–5.8 eV [38]. Formation of the oxygen vacancies leads to generation of additional electron states in the gap region. In the m-ZrO_2 bulk, the states are formed at approximately 0.5 and 0.2 eV below the edge of the conductive band for the ^4O_B and ^3O_B vacancies, respectively, showing the same trend as has been reported. [40] In the case of the surfaces, the position of the defect states seems to correlate with the location of the vacancy in the lattice. The separation between the states and the edge of the conducting band increases in a row $^2O_S < {}^3O_S < {}^3O_B < {}^4O_B$ for all studied surfaces regardless of the vacancy formation energy. The electronic states generated in the gap region may affect the performance of m-ZrO_2 as a support. Particularly, these states might be involved into the charge transfer at the metal–oxide interfaces.

3.3 Incorporation of Single Water Molecule

Next, we shifted our focus to molecular adsorption of a single water molecule onto each studied surface. In the case of the $(\bar{1}11)$ surface, adsorption of water onto surface sites is non-equivalent, although all surface zirconium atoms have identical coordination. The adsorption energy values range from -0.73 to -1.01 eV. The Zr–OH_2 bond length varies within 2.29–2.39 Å depending on the adsorption mode. The

different adsorption energies may be thus attributed to the formation of different hydrogen bonding networks depending on the surface site. Indeed, the strongest binding was observed when the water molecule formed a hydrogen bonding to the two-coordinated surface oxygen atom with the O–HOH distance of approximately 1.55 Å. In the case of the (011) and ($\bar{1}$01) surfaces, water adsorbs preferably on the five-coordinated zirconium atoms with the respective adsorption energies of −0.97 and −0.87 eV. The Zr–OH_2 bond lengths are similar to the case of the ($\bar{1}$11) surface and equal to 2.36 and 2.33 Å, respectively. On the ($\bar{1}$01) surface, water forms a close contact with the two-coordinated surface oxygen atom with the O–HOH distance of around 1.66 Å. Water adsorption on the six-coordinated zirconium atoms resulted in weaker binding. Fig. 4a summarizes the structures of the most favorable configurations of molecular water on the considered *m*-ZrO_2 surfaces.

We further considered the dissociative adsorption of a single water molecule. For each surface, the two-coordinated oxygen atom is involved into binding the hydrogen atom. Structures, where the hydrogen atom was bound to any of the three-coordinated oxygen atoms, are characterized by distinctly lower interaction energies. On the ($\bar{1}$11) surface, the hydroxyl species showed no preference of the surface zirconium atom, as reflected in the adsorption energies ranging from −0.99 to −1.09 eV, consistent with the earlier computational results. [30, 19]. On the two other surfaces, the hydroxyl species clearly favored interaction with the five-coordinated zirconium atoms, resulting in the dissociative adsorption energies of −1.97 and −1.54 eV for the (011) and ($\bar{1}$01) surfaces, respectively. The Zr–OH bond length varies insignificantly within 1.96–2.00 Å depending on the surface and adsorption site. Fig. 4b presents the most favorable *m*-ZrO_2/OH+H structures for the considered surfaces.

The molecular and dissociative adsorption of water on the ($\bar{1}$11) surface were found to be energetically equivalent, which might be linked to the formation of the hydrogen bonding that introduces additional stabilization. The equivalence is absent in the case of the (011) and ($\bar{1}$01) surfaces, where the lower coordination of the surface zirconium atoms seems to play a more contributing role into determining the adsorption strength. Furthermore, this effect is apparently stronger for the (011) surface as reflected in the values of the adsorption energy.

3.4 Stabilization of *m*-ZrO_2 Surfaces at Different Water Content

At higher surface coverage, it is more descriptive to discuss the stabilization of the corresponding *m*-ZrO_2 surfaces in terms of the surface energies in addition to the differental adsorption energies of water. The differental adsorption energy, δE, of a water molecule to a surface complex with n pre-adsorbed water molecules is calculated as follows:

$$\delta E = E_\Sigma(n+1) - (E_\Sigma(n) + E_\mathrm{W}), \quad (7)$$

where $E_\Sigma(x)$ is the total energy of a surface complex with x water molecules and E_W is the total energy of the isolated gas-phase molecule.

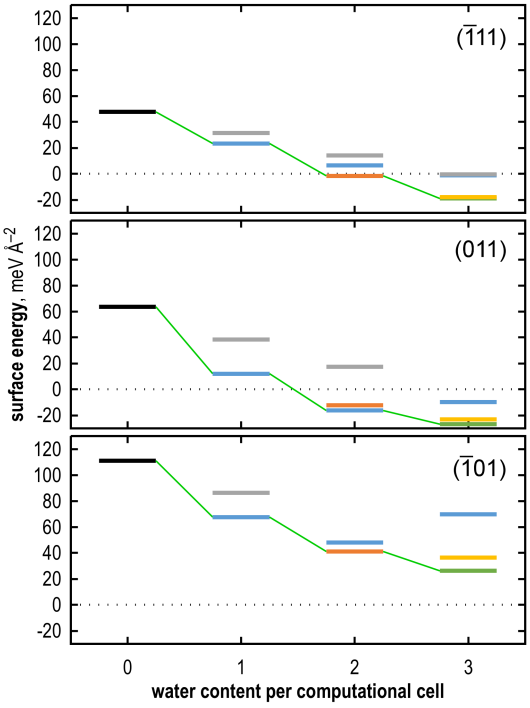

Fig. 5 Surface energies of the studied *m*-ZrO_2 surfaces as functions of the water content. Color coding emphasizes the degree of dissociation of water molecules: 0% in grey, 33% yellow, 50% in orange, 66% in green, 100% in blue. Green solid lines connect the most stable structures to highlight the trend. Surface energy values are given relative to the energies of the *m*-ZrO_2 bulk and the gas-phase water molecules (black dotted line).

Fig. 5 presents diagrams of the surface energies as functions of the water content, explicitly showing the degree of dissociation of water molecules in each considered case. For each water content, we considered all possible arrangements of the H_2O/OH+H species on the *m*-ZrO_2 surfaces, resulting in a screening set of over 380 structures, instead of adding water molecules to the most stable complexes with the lower surface coverage.

Simultaneous incorporation of two water molecules to the computational cells of the considered surfaces provides significantly greater stabilization compared to the incorporation of a single molecule. In the case of the ($\bar{1}$11) and (011) surfaces, the surface energy values lower beyond the level of the *m*-ZrO_2 bulk. Interestingly, the energy states corresponding to different degree of water dissociation are rel-

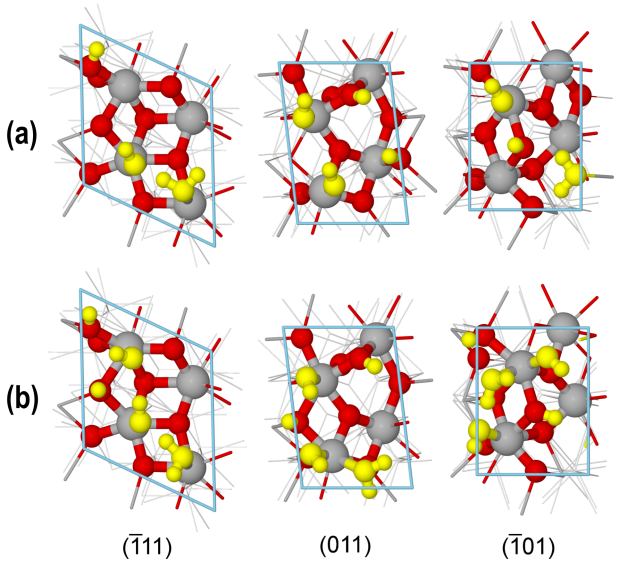

Fig. 6 Structures of the most favorable m-ZrO_2 complexes with (a) two and (b) three water molecules per computational cell for all studied surfaces. Color coding: Zr in grey, O in red, H_2O in yellow. The computational cells are shown in light blue. For the coordination of the surface atoms, the reader is kindly referred to Fig. 1.

atively close to each other with the maximum difference of <16 meV Å^{-2} for the most stable $(\bar{1}11)$ surface. For the less stable (011) and $(\bar{1}01)$ surfaces, only the states with 50% and 100% water dissociation are close. The energy level corresponding to completely molecular adsorption is found significantly higher for the (011) surface, while on the $(\bar{1}01)$ surface, we were unable to localize a structure with two water molecules adsorbed molecularly. Compared to the m-ZrO_2/OH+H systems, the added water preferably binds the $(\bar{1}11)$ and $(\bar{1}01)$ surfaces molecularly with the respective differential adsorption energies of -1.11 and -0.94 eV, which compare well to the values for molecular adsorption of a single water molecule. On the (011) surface, however, the added water preferably adsorbs dissociatively with the differential adsorption energy of about -1.09 eV. The values of the differential adsorption energy indicate that there is no significant interaction between the adsorbed water molecules or repulsion between them is counterpoised by the formation of the hydrogen bonding.

Simultaneous incorporation of three water molecules per each computational cell leads to complete hydration of the surfaces and, as the result, to their greatest stabilization. Unlike the $(\bar{1}11)$ and (011) surfaces, even complete hydration of the $(\bar{1}01)$ surface cannot lower its surface energy to the level of the m-ZrO_2 bulk. In the case of the $(\bar{1}11)$ surface, we localized the structures with all possible degrees of water dissociation, while for the (011) and $(\bar{1}01)$ surfaces, we were unable to localize the structures corresponding to completely molecular adsorption of water. The span of the energy levels due to the different water dissociation decreases in a row $(\bar{1}01) > (\bar{1}11) \approx (011)$ as $43.6 > 18.7 \approx 17.1$ meV Å^{-2}. The most stable configurations correspond to the 33% and 66% water dissociation and are energetically very close. For the $(\bar{1}11)$ surface, the difference is <1.0 meV Å^{-2}, and the structures may be assumed to be in a thermodynamic equilibrium. Compared to the surfaces with two water molecules, the added water binds the $(\bar{1}11)$ and $(\bar{1}01)$ surfaces dissociatively with the respective adsorption energies of -0.78 and -0.53 eV, whereas it adsorbs on the (011) molecularly with the adsorption energy of approximately -0.40 eV. In these cases, the lowered values of the differential adsorption energy suggest that at the highest surface coverage, the formation of hydrogen bonding is insufficient to cancel the repulsion between the adsorbed water molecules.

Overall, our results show that the greatest stabilization of the m-ZrO_2 surfaces is achieved upon complete hydration. The most stable configurations of water on the surfaces typically require a part of the molecules to be dissociated regardless of the water content. Fig. 6 assembles the structures of the m-$ZrO_2/(H_2O)_{2–3}$ complexes that provide the greatest stabilization of the respective surfaces. The gradual decay in the differential adsorption energies upon increase of the water content might suggest that addition of the forth molecule to the computational cells would provide even weaker stabilization, since the molecule would only physisorb and form a multilayer structure via hydrogen bonding.

The most stable configurations of water in terms of the dissociation degree change with the increasing water content in the following rows: 100% – 50% – 66% on the $(\bar{1}11)$ and $(\bar{1}01)$ surfaces and 100% – 100% – 66% on the (011) surface. In the latter case, water molecules have a greater tendency to dissociate, resulting in higher concentration of the surface hydroxyl groups.

The density of states of the m-ZrO_2 surfaces (Fig. 3) changes insignificantly upon incorporation of water. The changes in the band gaps are thereby <0.1 eV.

3.5 Phase Diagrams for m-$ZrO_2/(H_2O)_n$ Systems

Twelve representative complexes of the m-ZrO_2 surfaces with water (Figs. 4 and 6) were used to construct the phase diagrams shown in Fig. 7. A temperature range between 600 and 900 K was considered in the evaluations to represent the pre-treatment and/or reaction conditions.

Our findings suggest that the $(\bar{1}11)$ surface remains preferably bare at the partial water pressures <1 bar within the considered temperature range. On the other hand, the (011) and $(\bar{1}01)$ surfaces seem to begin interacting with water already at lower pressures, forming thereby structures shown in Fig. 4a. At the temperature of 600 K, all studied surfaces are expected to incorporate more water and form the

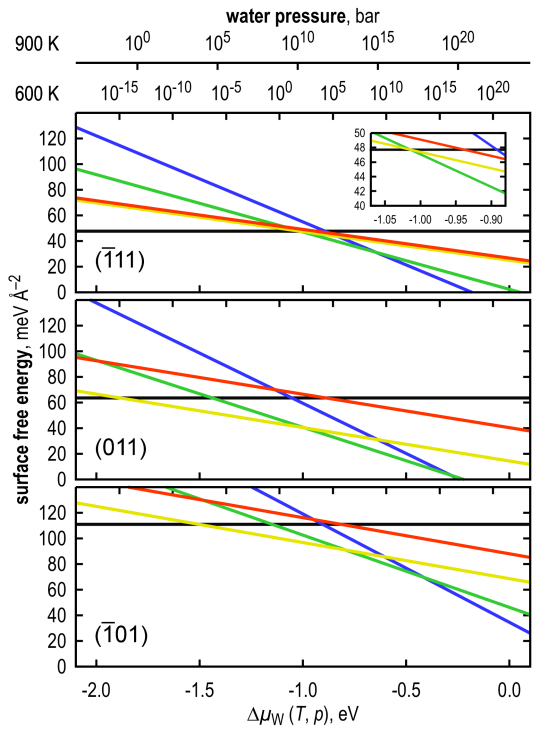

Fig. 7 Phase diagrams the studied m-ZrO_2 surfaces with different water content. Color coding: plain surfaces in black, structures from Fig. 4a in red, structures from Fig. 4b in yellow, structures from Fig. 6a in green, and structures from Fig. 6b in blue. Surface free energy values are given relative to the energies of the m-ZrO_2 bulk and the gas-phase water molecules.

structures shown in Fig. 6a at the elevated water pressures of 10^0–10^6 bar. At higher temperature regimes, adoption of such structures is less feasible as it requires extremely high water pressure. Complete hydration of the studied surface is also non-achievable within the considered temperature range. Upon the temperature decrease, the ($\bar{1}$11), (011), and ($\bar{1}$01) surfaces of the m-ZrO_2 are likely to quickly uptake water. At room temperature and atmospheric water pressure, all studied surfaces are expected to be fully hydrated and adopt structures shown in Fig. 6b.

Our results indicate that formate formation from CO is more likely to occur on the (011) and ($\bar{1}$01) surfaces, which provide surface hydroxyl groups at the considered reaction conditions. Formation of the formate species is evident from the experiments; [20] however, there are possibilities for other oxygenates, such as e. g. carboxyl, HCO, and CO_2, to be formed. The relative abundance of these facets should be low, due to their higher surface energies compared to the most stable ($\bar{1}$11) surface. However, presence of surface oxygen vacancies may alter reactivity of the surfaces towards water and promote formation of the surface hydroxyl groups. Moreover, the edges and corners of the m-ZrO_2 crystallites, providing different types of the surface sites, could be responsible for interaction of CO with dissociated water.

4 Conclusions

Here, we reported a combined first-principles and atomistic thermodynamics study on the structure and stability of the selected low-index m-ZrO_2 surfaces in presence of oxygen vacancies and water. Oxygen vacancies were found to be the most stable in the subsurface layers of the ($\bar{1}$11) and (011) surfaces at the four-coordinated lattice oxygen atoms, which is similar to the case of the m-ZrO_2 bulk. In contrast, the most favorable location for an oxygen vacancy in the ($\bar{1}$01) surface was identified in the surface atomic layer at the point to the three-coordinated lattice oxygen. The formation energies of the most stable vacancies showed a strong linear dependence on the corresponding surface energy, making the most stable ($\bar{1}$11) surface the least accessible for the oxygen vacancies and the least stable ($\bar{1}$01) surface the most.

Next, we gradually incorporated water molecules into the studied surfaces, varying the dissociation state of water for each water content. Accounting for all possible combinations of molecular and dissociated water resulted in a screening set of over 380 structures. Our results indicate that water provides stabilization of the ($\bar{1}$11) and (011) surfaces to the levels beyond the m-ZrO_2 bulk in contrast to the ($\bar{1}$01) surface, where such stabilization is non-achievable. Moreover, the greatest stabilization of the surfaces was observed when a part of the incorporated water was dissociated. Upon complete hydration of the surfaces, the requirement for water to be partly dissociated becomes stronger for the less stable (011) and ($\bar{1}$01) surfaces, whereas the most stable ($\bar{1}$11) surface is stabilized equally well regardless of the dissociation state of water.

Analysis of the phase diagrams suggested that the ($\bar{1}$11) surface preferably remains clean under the water pressures $<$1 bar within the 600–900 K temperature range. In contrary, the (011) and ($\bar{1}$01) surfaces are likely to bind minimal amount of water at the aforementioned conditions. Upon increase of the water pressure, all considered surface are expected to incorporate more water; nonetheless, complete hydration seems to be unfeasible within the considered temperature range. At room temperatures, all surfaces are possibly fully hydrated with approximately 66% of the adsorbed H_2O molecules dissociated.

Overall, our findings provide a deeper atomic-level insight in the structure and stability of the m-ZrO_2 surfaces in water-rich environment at the pre-treatment and/or reaction conditions. Construction and analysis of the phase diagrams based on the comprehensive screening of the structures not only generate a connection point between the theory and experiment but also constitute a useful tool for prediction of the surface structure, particularly, when selecting a suitable

model for studying catalyst–support interactions under the pre-treatment and/or reaction conditions.

Acknowledgements We gratefully acknowledge the financial support from the Academy of Finland (grant 277222). Electronic structure calculations were made possible through the use of computational resources provided by the CSC – IT Center of Science in Espoo, Finland (http://www.csc.fi/). We thank Dr. Jaana Kanervo and Prof. Leon Lefferts for fruitful discussions.

References

1. (2013) NIST-JANAF thermochemical tables. URL http://kinetics.nist.gov/janaf/
2. Chauke HR, Murovhi P, Ngoepe PE, de Leeuw NH, Grau-Crespo R (2010) Electronic structure and redox properties of the Ti-doped zirconia (111) surface. J Phys Chem C 114:15,403–15,409, DOI 10.1021/jp103181q
3. Chen HT, Chang JG (2010) Oxygen vacancy formation and migration in $Ce_{1-x}Zr_xO_2$ catalyst: A DFT+U calculation. J Chem Phys 132:214,702, DOI 10.1063/1.3429314
4. Contreras JL, Salmones J, Colín-Luna JA, Nuño L, Quintana B, Córdova I, Zeifert B, Tapia C, Fuentes GA (2014) Catalysts for H_2 production using the ethanol steam reforming (a review). Int J Hydrogen Energy 39:18,835–18,853, DOI 10.1016/j.ijhydene.2014.08.072
5. Ding H, Virkar AV, Liu F (2012) Defect configuration and phase stability of cubic versus tetragonal yttria-stabilized zirconia. Solid State Ionics 215:16–23, DOI 10.1016/j.ssi.2012.03.014
6. Enkovaara J, C R, Mortensen JJ, Chen J, Dułak M, Ferrighi L, Gavnholt J, Glinsvad C, Haikola V, Hansen HA, Kristoffersen HH, Kuisma M, Larsen AH, Lehtovaara L, Ljungberg M, Lopez-Acevedo O, Moses PG, Ojanen J, Olsen T, Petzold V, Romero NA, Stausholm-Møller J, Strange M, Tritsaris GA, Vanin M, Walter M, Hammer B, Häkkinen H, Madsen GKH, Nieminen RM, Nørskov JK, Puska M, Rantala TT, Schiøtz J, Thygesen KS, Jacobsen KW (2010) Electronic structure calculations with gpaw: A real-space implementation of the projector augmented-wave method. J Phys: Condens Matter 22:253,202, DOI 10.1088/0953-8984/22/25/253202
7. Foster AS, Sulimov VB, Gejo FL, Shluger AL, Nieminen RM (2001) Structure and electrical levels of point defects in monoclinic zirconia. Phys Rev B 64:224,108, DOI 10.1103/PhysRevB.64.224108
8. Ganduglia-Pirovano MV, Hofmann A, Sauer J (2007) Oxygen vacancies in transition metal and rare earth oxides: Current state of understanding and remaining challenges. Surf Sci Rep 62:219–270, DOI 10.1016/j.surfrep.2007.03.002
9. Graf PO, Mojet BL, van Ommen JG, Lefferts L (2007) Comparative study of steam reforming of methane, ethane and ethylene on Pt, Rh and Pd supported on yttrium-stabilized zirconia. Appl Catal A 332:310–317, DOI 10.1016/j.apcata.2007.08.032
10. Graf PO, Mojet BL, Lefferts L (2008) Influence of potassium on the competition between methane and ethane in steam reforming over Pt supported on yttrium-stabilized zirconia. Appl Catal A 346:90–95, DOI 10.1016/j.apcata.2008.05.010
11. Han Y, Zhu J (2013) Surface science studies on the zirconia-based model catalysts. Top Catal 56:1525–1541, DOI 10.1007/s11244-013-0156-5
12. Harju H, Lehtonen J, Lefferts L (2015) Steam- and autothermal-reforming of *n*-butanol over Rh/ZrO_2 catalyst. Catal Today 244:47–57, DOI 10.1016/j.cattod.2014.08.013
13. Harju H, Lehtonen J, Lefferts L (2016) Steam reforming of *n*-butanol over Rh/ZrO_2 catalyst: role of 1-butene and butyraldehyde. Appl Catal B 182:33–46, DOI 10.1016/j.apcatb.2015.09.009
14. Hoang TMC, Rao NK, Lefferts L, Seshan K (2015) Investigation of Ce–Zr oxide-supported Ni catalysts in the steam reforming of *meta*-cresol as a model component for bio-derived tar. Chem Cat Chem 7:468–478, DOI 10.1002/cctc.201402857
15. Ignatchenko A, Nealon DG, Dushane R, Humphries K (2006) Interaction of water with titania and zirconia surfaces. J Mol Catal A: Chem 256:57–74, DOI 10.1016/j.molcata.2006.04.031
16. Ignatchenko AV (2011) Density functional theory study of carboxylic acids adsorption and enolization on monoclinic zirconia surfaces. J Phys Chem C 115:16,012–16,018, DOI 10.1021/jp203381h
17. Jiang N, Burri A, Park SE (2016) Ethylbenzene to styrene over ZrO_2-based mixed metal oxide catalysts with CO_2 as soft oxidant. Chin J Catal 37:3–15, DOI 10.1016/S1872-2067(15)60901-9
18. Jomard G, Petit T, Pasturel A, Magaud L, Kresse G, Hafner J (1999) First-principles calculations to describe zirconia pseudopolymorphs. Phys Rev B 59:4044–4052, DOI 10.1103/PhysRevB.59.4044
19. Korhonen ST, Catalayud M, Krause AOI (2008) Stability of hydroxylated $(\bar{1}11)$ and $(\bar{1}01)$ surfaces of monoclinic zirconia: A combined study by DFT and infrared spectroscopy. J Phys Chem C 112:6469–6476, DOI 10.1021/jp8008546
20. Kouva S, Andersin J, Honkala K, Lehtonen J, Lefferts L, Kanervo J (2014) Water and carbon oxides on monoclinic zirconia: experimental and computational insights. Phys Chem Chem Phys 16:20,650–20,664, DOI 10.1039/c4cp02742f

21. Kouva S, Honkala K, Lefferts L, Kanervo J (2015) Review: monoclinic zirconia, its surface sites and their interaction with carbon monoxide. Catal Sci Technol 5:3473–3490, DOI 10.1039/C5CY00330J
22. Liu T, Zhang X, Yuan L, Yu J (2015) A review of high-temperature electrochemical sensors based on stabilized zirconia. Solid State Ionics 283:91–102, DOI 10.1016/j.ssi.2015.10.012
23. McCullough JD, Trueblood KN (1959) The crystal structure of baddeleyite (monoclinic ZrO_2). Acta Crystallogr 12:507–511, DOI 10.1107/S0365110X59001530
24. Mortensen JJ, Hansen LB, Jacobsen KW (2005) Real-space grid implementation of the projector augmented wave method. Phys Rev B 71:035,109, DOI 10.1103/PhysRevB.71.035109
25. Nahar G, Duport V (2014) Hydrogen production from simple alkanes and oxygenated hydrocarbons over ceria–zirconia supported catalysts: Review. Renew Sustainable Energy Rev 32:777–796, DOI 10.1016/j.rser.2013.12.040
26. Pacchioni G (2014) Ketonization of carboxylic acids in biomass conversion over TiO_2 and ZrO_2 surfaces: A DFT perspective. ACS Catal 4:2874–2888, DOI 10.1021/cs500791w
27. Perdew JP, Burke K, Ernzerhof M (1996) Generalized gradient approximation made simple. Phys Rev Lett 77:3865–3868, DOI 10.1103/PhysRevLett.77.3865
28. Perdew JP, Burke K, Ernzerhof M (1997) Generalized gradient approximation made simple [phys. rev. lett. 77, 3865 (1996)]. Phys Rev Lett 78:1396–1396, DOI 10.1103/PhysRevLett.78.1396
29. Pintos DG, Juan A, Irigoyen B (2012) Oxygen vacancy formation on the $Ni/Ce_0 \cdot 75Zr_0 \cdot 25O_2(111)$ surface. a DFT+U study. Int J Hydrogen Energy 37:14,937–14,944, DOI 10.1016/j.ijhydene.2011.12.079
30. Piskorz W, Grybos J, Zasada F, Cristol S, Paul JF, Adamski A, Sojka Z (2011) Periodic DFT and atomistic thermodynamic modeling of the surface hydration equilibria and morphology of monoclinic ZrO_2 nanocrystals. J Phys Chem C 115:24,274–24,286, DOI 10.1021/jp2086335
31. Piskorz W, Grybos J, Zasada F, Zapala P, Cristol S, Paul JF, Sojka Z (2012) Periodic DFT study of the tetragonal ZrO_2 nanocrystals: Equilibrium morphology modeling and atomistic surface hydration thermodynamics. J Phys Chem C 116:19,307–19,320, DOI 10.1021/jp3050059
32. Prakash BS, Kumar SS, Aruna ST (2014) Properties and development of Ni/ysz as an anode material in solid oxide fuel cell: A review. Renew Sustainable Energy Rev 36:149–179, DOI 10.1016/j.rser.2014.04.043
33. Raz S, Sasaki K, Maier J, Riess I (2001) Characterization of adsorbed water layers on Y_2O_3-doped ZrO_2. Solid State Ionics 143:181–204, DOI 10.1016/S0167-2738(01)00826-8
34. Reuter K, Scheffler M (2001) Surface core-level shifts at an oxygen-rich Ru surface: O/Ru(0001) vs. $RuO_2(110)$. Surf Sci 490:20–28, DOI 10.1016/S0039-6028(01)01214-6
35. Reuter K, Scheffler M (2002) Composition, structure, and stability of $RuO_2(110)$ as a function of oxygen pressure. Phys Rev B 65:035,406, DOI 10.1103/PhysRevB.65.035406
36. Reuter K, Scheffler M (2003) First-principles atomistic thermodynamics for oxidation catalysis: Surface phase diagrams and catalytically interesting regions. Phys Rev B 90:046,103, DOI 10.1103/PhysRevLett.90.046103
37. Rioche C, Kulkarni S, Meunier FC, Breen JP, Burch R (2005) Steam reforming of model compounds and fast pyrolysis bio-oil on supported noble metal catalysts. Appl Catal B 61:130–139, DOI 10.1016/j.apcatb.2005.04.015
38. Robertson J (2004) High dielectric constant oxides. Eur Phys J Appl Phys 28:265–291, DOI 10.1051/epjap:2004206
39. Sangalli D, Lamperti A, Cianci E, Ciprian R, Perego M, Debernardi A (2013) Role of oxygen vacancies on the structure and density of states of iron-doped zirconia. Phys Rev B 87:085,206, DOI 10.1103/PhysRevB.87.085206
40. Syzgantseva OA, Calatayud M, Minot C (2012) Revealing the surface reactivity of zirconia by periodic DFT calculations. J Phys Chem C 116:6636–6644, DOI 10.1021/jp209898q
41. Wang H, Li G, Xue Y, Li L (2007) Hydrated surface structure and its impacts on the stabilization of *t*-ZrO_2. J Solid State Chem 180:2790–2797, DOI 10.1016/j.jssc.2007.08.015
42. Yashima M, Hirose T, Katano S, Suzuki Y, Kakihana M, Yoshimura M (1995) Structural changes of ZrO_2–CeO_2 solid solutions around the monoclinic-tetragonal phase boundary. Phys Rev B 51:8018–8025, DOI 10.1103/PhysRevB.51.8018
43. Youssef M, Yildiz B (2012) Intrinsic point-defect equilibria in tetragonal ZrO_2: Density functional theory analysis with finite-temperature effecs. Phys Rev B 86:114,109, DOI 10.1103/PhysRevB.86.144109
44. Zhu J, van Ommen JG, Lefferts L (2006) Effect of surface oh groups on catalytic performance of yittrium-stabilized ZrO_2 in partial oxidation of CH_4 to syngas. Catal Today 117:163–167, DOI 10.1016/j.cattod.2006.05.046